High-Performance Nanogap Photodetectors Based on 2D Halide Perovskites with a Novel Spacer Cation

Yi Shen, Linqu Luo, Yuxuan Zhang, You Meng, Yan Yan, Pengshan Xie, Dengji Li, Yu Ji, Siliang Hu, SenPo Yip, Zhengxun Lai,* Thomas D. Anthopoulos, and Johnny C. Ho*

2D Ruddlesden—Popper (RP) halide perovskites are attracting increasing research interest due to their enhanced stability compared to 3D perovskites. However, the quantum confinement effect of bulk organic spacers hinders the separation and transport of photo-generated carriers. Here, a multiple aromatic ring spacer, 3-benzothiophene methylammonium (BTMA), is developed for a new 2D RP perovskite. The BTMA spacer is demonstrated, with a significant dipole moment, can impair the influence of the quantum confinement effect, and the presence of S atoms or thiophene is favorable for enhancing the interaction between organic spacers and inorganic sheets, improving the stability of perovskites. The perovskite photodetector with BTMA as spacers displays higher device performance than the control sample with 1-naphthalene methylammonium (NMA) as spacers. Importantly, the outstanding stability of BTMA-based perovskite films and devices is also confirmed under moisture, heat, and illumination conditions. Combining the asymmetric coplanar nanogap electrode architecture, the photodetectors' enhanced responsivity, detectivity, and external quantum efficiency of 314 A W^{-1}, 3.4×10^{13} Jones, and 865%, respectively, are demonstrated. Importantly, the nanogap photodetectors display promising self-power characteristics, which makes them attractive for numerous energy-efficient applications. The work highlights a new route toward developing high-performance 2D RP perovskite-based photodetectors with excellent long-term stability.

1. Introduction

In recent years, halide perovskites (ABX_3, A is Cs^+ or CH_3NH^{3+}; B is Pb^{2+} or Sn^{2+}; X is halogen) have been garnering increasing attention due to their exceptional photovoltaic conversion capabilities, which rival or even exceed those of silicon-based devices.[1–6] However, the further commercialization of the halide perovskites is hindered by their poor stability.[7,8] A promising strategy to enhance their stability is using large-volume hydrophobic amine ions to transform the 3D halide perovskites into a 2D structure.[9–11]

Ruddlesden—Popper (RP) halide perovskites (R_2BX_4, R is a bulky monoamine) are a significant category in 2D perovskites and have been extensively researched.[12–14] However, the energy level of these inserted organic spacer layers is misaligned with that of the inorganic octahedral layers, which results in a diminished interlayer transport capability for photo-generated electrons and holes in 2D halide perovskites.[15,16] Developing spacers with high dipole moments and suitable volume

Y. Shen, Y. Zhang, Y. Meng, Y. Yan, P. Xie, D. Li, S. Hu, J. C. Ho
Department of Materials Science and Engineering
City University of Hong Kong
Kowloon, Hong Kong SAR 999077, China
E-mail: johnnyho@cityu.edu.hk

L. Luo, T. D. Anthopoulos
Physical Science and Engineering Division
King Abdullah University of Science and Technology
Thuwal 23955-6900, Saudi Arabia

Y. Ji
School of Optoelectronic Science and Engineering
University of Electronic Science and Technology of China (UESTC)
Chengdu 610054, China

S. Yip
Institute for Materials Chemistry and Engineering
Kyushu University
Fukuoka 816-8580, Japan

Z. Lai
College of Semiconductors (College of Integrated Circuits)
Hunan University
Changsha 410082, China
E-mail: zxlai3-c@my.cityu.edu.hk

T. D. Anthopoulos
Henry Royce Institute
Photon Science Institute
Department of Electrical and Electronic Engineering
The University of Manchester
Manchester M13 9PL, UK

J. C. Ho
State Key Laboratory of Terahertz and Millimeter Waves
City University of Hong Kong
Kowloon, Hong Kong SAR 999077, China

**ADVANCED
SCIENCE NEWS**

www.advancedsciencenews.com

**ADVANCED
FUNCTIONAL
MATERIALS**

www.afm-journal.de

is considered an effective strategy to enhance the performance of 2D perovskite devices.[17] So far, the reported monoamine cations are mainly single aromatic ring cations and aliphatic cations, such as propylammonium (PA),[18] isobutylammonium (*i*BA)[19] and phenylethylammonium (PEA).[11] Aromatic spacers always have more significant polarity and conjugation than aliphatic spacers, which leads to their high electrical conductivity and weakened quantum confinement effect in 2D RP perovskites.[14] Moreover, multiple aromatic ring spacers with extensive π-electron delocalization in the conjugated framework can further promote the carrier transport capability in 2D perovskites.[20–24] In previous reports, Passarelli et al. incorporated naphthalene-, pyrene-, and perylene-based spacers into 2D perovskites with the n value of 1 and found their excellent out-of-plane conductivity.[21] Xu et al. used 1-naphthalene methylammonium and 9-anthracene methylammonium as spacer cations of 2D perovskites and achieved impressive power conversion efficiency (PCE) for corresponding solar cells with long-term stability.[23] Subsequently, 1-naphthylamine (1-NA) was developed as spacers by Jin et al.[24] They pointed out that the strong π-π interaction of naphthylamine can stabilize the perovskite lattices and enhance the quality of perovskite films simultaneously. Notably, the commonly used multiple aromatic ring spacers in photoelectric devices are mainly naphthyl-based, especially in light-emitting diodes. The study for other multiple aromatic ring spacers remains unexplored.

Apart from the inherent properties of perovskite materials, the influence of the device structure on the performance is also significant. For photodetectors, the typical structure is a vertical type, but it has a special requirement for selecting transparent electrodes. The other coplanar structure is convenient to fabricate photodetectors. Furthermore, for this structure, the reduction of inter-electrode distance can achieve a significant enhancement in device performance. Also, in recent years, a novel adhesion lithography technique was developed to prepare nanogap coplanar electrodes, which have been widely used in diodes, field-effect transistors, and photodetectors owing to their low cost and high device performance.[25,26] However, few studies have been reported on photodetectors with ultra-narrow nanogap between electrodes based on layered 2D perovskites.

Therefore, in this work, we designed and synthesized a novel multiple aromatic ring spacer, 3-benzothiophene methylammonium (BTMA), and used it to configure a new kind of layered perovskite. Compared with a 1-naphthalene methylammonium (NMA) spacer, introducing an S atom or single thiophene increases the molecule's polarity. It reinforces the interaction between organic spacers and inorganic PbI$_6$ sheets in 2D perovskites. The device performance of BTMA-based perovskite photodetector is demonstrated to be superior to that of the NMA-based perovskite photodetectors while exhibiting better stability under moisture, heat, and illumination conditions. Furthermore, the utilization of nanogap electrodes in BTMA-based perovskite photodetectors significantly promotes the properties of devices, and the responsivity, detectivity, and external quantum efficiency can reach high values of 314 A W^{-1}, 3.4×10^{13} Jones and 865%, respectively. This work offers a strategy for promoting the optoelectronic properties of 2D RP perovskite photodetectors.

2. Results and Discussion

Previous reports have proved that the S atom or thiophene can strengthen the electric coupling between organic layers and octahedral sheets, stabilizing the perovskite lattices.[27–29] Inspired by this character, we intelligently designed and synthesized a new monoamine cation with a long-conjugated length, 3-benzothiophene methylammonium (BTMA). For this spacer, its superiority is mainly reflected in the following three aspects, as shown in **Figure 1a**: i) The extensive delocalization of π-electron that BTMA possesses can contribute to its enhanced conductivity compared with single aromatic ring spacers.[21] ii) The anticipated low symmetry is expected to endow the BTMA spacer with greater polarity in favor of mitigating the impact of quantum confinement effects in 2D RP perovskites and enhancing the transport of carriers. iii) More importantly, the presence of S atom in the thiophene ring is expected to further increase the stability of RP perovskites by reinforcing the interaction of spacers with PbI$_6$ sheets.

To demonstrate the superiority of the BTMA spacer, we used 1-naphthalene methylammonium (NMA) as the control sample. We prepared the 2D RP perovskites, BTMA$_2$PbI$_4$ and NMA$_2$PbI$_4$, named BTMA-Pb and NMA-Pb, respectively. Density Functional Theory (DFT) was employed to study molecules' structure and dipole moment. Figure 1b shows the chemical structures and electrostatic potential (ESP) maps of BTMA and NMA spacers. As expected, the calculated dipole moment of the BTMA spacer is 1.73 D, more significant than that of the NMA spacer (1.43 D). The higher polarity of the BTMA spacer is believed to increase the dielectric constant, thereby weakening the dielectric mismatch between organic and inorganic PbI$_6$ layers.[15,30] Also, the increased polarity can potentially reduce the exciton binding energy of 2D RP perovskites and facilitate the separation and transport of photogenerated carriers.[30] To prove the regulation effect of the BTMA spacer, the relative dielectric constants of BTMA-Pb and NMA-Pb films were measured through an impedance analyzer. The results are shown in Figure S7, Supporting Information, where the dielectric constants of BTMA-Pb and NMA-Pb films are ≈6.6 and ≈6.1, proving that the introduction of BTMA spacer can increase the dielectric constant of 2D perovskites. Besides, compared to the NMA spacer's benzene ring, the BTMA spacer's thiophene on the NH^{3+} side has a smaller volume, which is beneficial for a tighter binding with inorganic PbI$_6$ octahedrons. This is well proved by the calculated perovskite structures for BTMA-Pb and NMA-Pb. Figure S5, Supporting Information, shows that the penetration depth (defined by the distance of nitrogen atom of NH$_3^+$ with the plane of I atoms of inorganic PbI$_6$ sheets) of simulated structure for BTMA-Pb and NMA-Pb are 0.435 and 0.405 Å, respectively.[31] The deeper depth suggests that the NH^{3+} of BTMA spacer has a stronger bond with PbI$_6$ octahedrons. To further investigate the interaction between the spacers and perovskite sheets, X-ray photoelectron spectroscopy (XPS) was conducted on the BTMA-Pb and NMA-Pb perovskite films. The results are displayed in Figure 1c, in which the main peaks for Pb are found at 137.6 and 142.5 eV for BTMA-Pb films, while the corresponding peaks of NMA-Pb films are observed at 137.8 and 142.6 eV. These two peaks can be assigned to the Pb 4f$_{7/2}$ and Pb 4f$_{5/2}$, respectively. The apparent shift toward lower binding energy of BTMA-Pb films suggests the different chemical
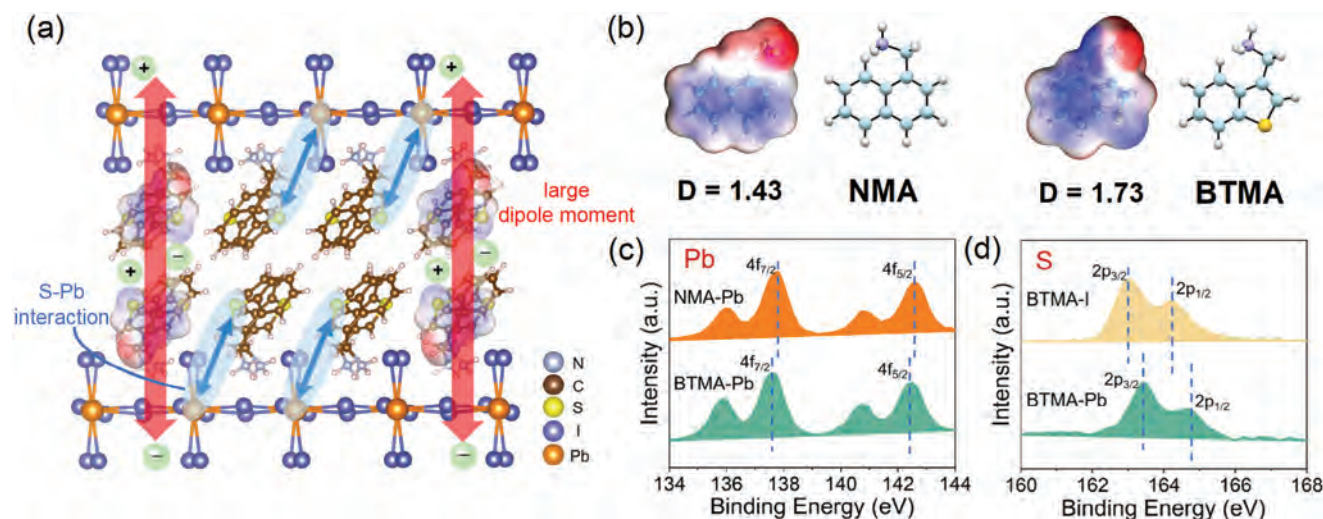
Figure 1. a) Schematic diagram for interaction between BTMA spacers and inorganic PbI_6 sheets. b) The chemical structure and ESP of NMA and BTMA spacers. c,d) The XPS spectrum of Pb 4f for the NMA-Pb and BTMA-Pb films and S 2p for the BTMA-I powder and the BTMA-Pb film.

environment for Pb atoms, possibly caused by more vital interaction between BTMA spacers and PbI_6 octahedral sheets compared with the NMA-Pb films. Meanwhile, additional tests on the binding energy (shown in Figure 1d) of S atoms in BTMA-Pb films and BTMA-I powder (3-benzothiophene methylamine iodide power, which is used to prepare perovskite precursor solution) reveal that the S 2p peaks of the latter have higher binding energy in BTMA-Pb films, which also suggests the strong interaction between BTMA spacers and PbI_6 octahedrons.[28] This enhanced interaction is expected to stabilize the RP perovskite lattices better.

It is well-known that crystallinity is a crucial factor affecting the properties of 2D RP perovskite films. Therefore, X-ray diffraction (XRD) was measured to study the crystallinity of BTMA-Pb and NMA-Pb perovskite films. **Figure 2a** shows the XRD peaks of BTMA-Pb and NMA-Pb perovskite films, and the corresponding simulated XRD curves can be seen in Figure S6, Supporting Information. Both BTMA-Pb and NMA-Pb film samples show strong XRD intensities, indicating their high crystallinity. Combined with the calculated XRD maps for BTMA-Pb and NMA-Pb perovskite lattices, all these peaks can be assigned to the (00n) planes, as Figure 2a shows, which suggests highly oriented growth of these films along the direction of [001]. As we know, it is slow for carriers to transport in organic layers or transport between organic layers and inorganic layers in 2D perovskite lattices. Therefore, the highly ordered growth direction of BTMA-Pb and NMA-Pb perovskite lattices can provide the condition for photo-generated carriers to transport in inorganic PbI_6 layers as much as possible, thereby promoting the collection of the charges and enhancing the optoelectronic properties (Figure 2b). Additionally, the UV–vis absorption of BTMA-Pb and NMA-Pb perovskite films was also analyzed, and the spectrum is shown in Figure 2c. Only one sharp absorption edge is observed around 500 nm for BTMA-Pb and NMA-Pb films, manifesting their pure phase of 2D perovskites. The band gaps for BTMA-Pb and NMA-Pb perovskite films can be determined to be around 2.38 and 2.40 eV, respectively, through the analysis for the corresponding

Tacu plot shown (Figure S9, Supporting Information). Moreover, the results of the photoluminescence (PL) spectrum for BTMA-Pb and NMA-Pb films under an excitation laser with 450 nm wavelength are shown in Figure 2d. The main peaks appear around 525 nm for two samples. As we know, better crystallinity always leads to a narrower PL peak and is advantageous for carriers' transport. In this case, it is worth noting that the full-width at half-maximum (FWHM) of the PL peak of BTMA-Pb film is narrower than that of NMA-Pb film, which indicates the more excellent crystallinity for BTMA-Pb film. To further study the crystallinity and morphology of BTMA-Pb and NMA-Pb perovskite films, we conducted the measurement of scanning electron microscopy (SEM) and atomic force microscopy (AFM) on these two films. From the SEM images in Figure 2e, it can be observed that the NMA-Pb perovskite film has many cracks, which is detrimental to the transport of charge carriers. However, the BTMA-Pb perovskite film has a rugged surface but is very dense and continuous, benefiting the carrier transport in perovskite lattices. What's more, a low value of 2.59 nm is obtained for the root-mean-square (RMS) roughness of BTMA-Pb perovskite film, smaller than that of NMA-Pb perovskite film (RMS = 11.9 nm), as shown in AFM results of Figure 2f. These characterizations demonstrate that the BTMA-Pb perovskite possesses superior crystallinity and film quality, potentially providing it with better photoelectric performance.

Subsequently, the BTMA-Pb and NMA-Pb perovskite films were fabricated into photodetectors to explore their photoelectric performance in detail. The structure of photodetectors is shown in Figure S10, Supporting Information, wherein two gold electrodes are deposited onto the 2D perovskite film. The active area of the photodetectors is stimulated using a laser light source (450 nm). The current–voltage (I–V) curves for these photodetectors were evaluated under varying light intensities, as well as in the absence of light, as shown in **Figure 3a,b**. It is noted that the x-axis intersection shifts of I–V curves are possibly caused by the ionic migration of perovskites, which always leads to the formation of the internal electric field.[32] The on/off radio for
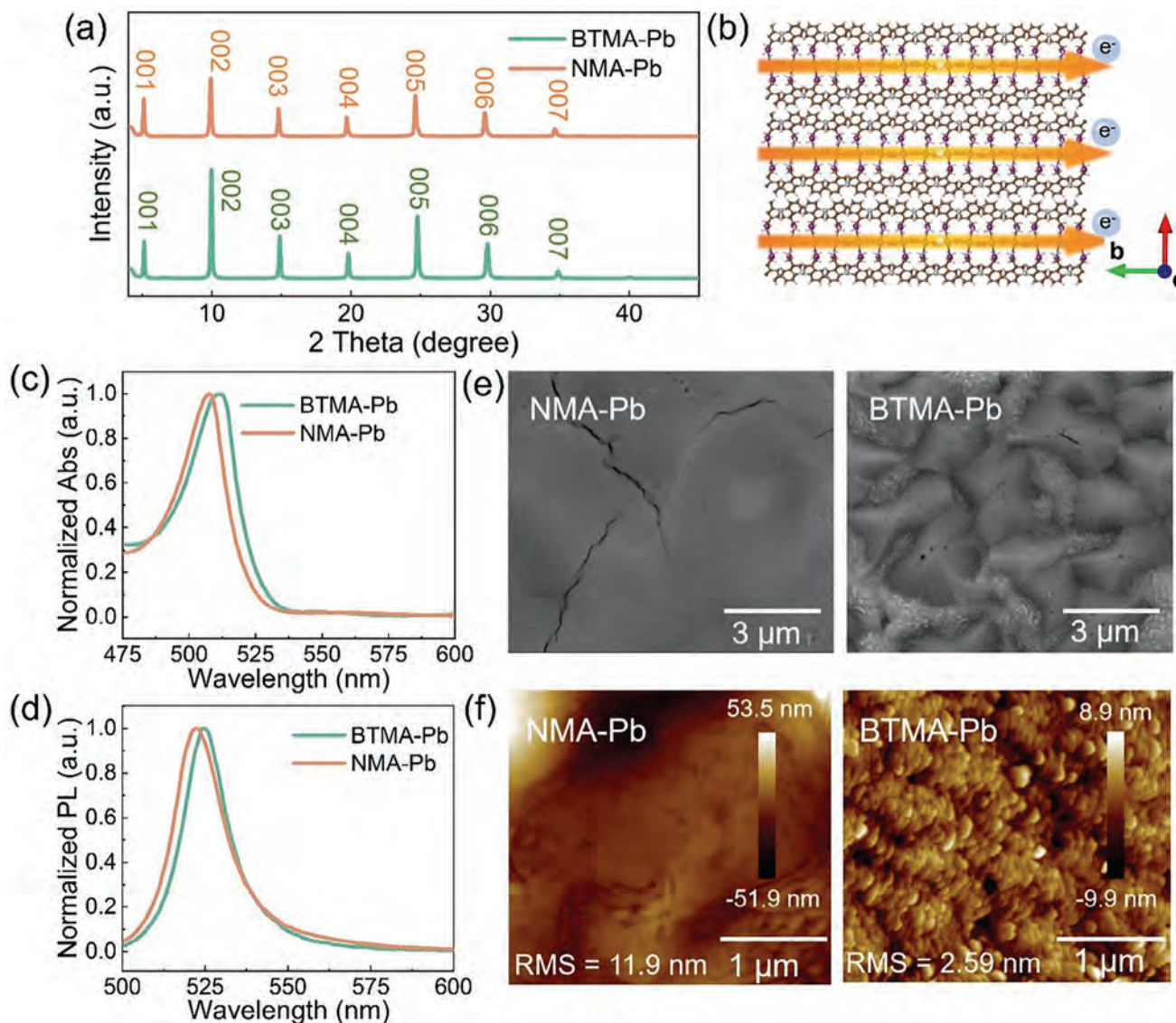
**ADVANCED
SCIENCE NEWS**

www.advancedsciencenews.com

**ADVANCED
FUNCTIONAL
MATERIALS**

www.afm-journal.de

Figure 2. a) XRD of the BTMA-Pb and NMA-Pb films. b) Schematic diagram of the carrier transfer in highly ordered perovskite lattices. c) UV–Vis absorption spectrum of the BTMA-Pb and NMA-Pb films. d) PL spectrum of the BTMA-Pb and NMA-Pb films. e) SEM images of the BTMA-Pb and NMA-Pb films. f) AFM images of the BTMA-Pb and NMA-Pb films.

BTMA-Pb and NMA-Pb photodetectors can reach a high value of 10^3. Besides, the linear results of I–V curves (Figure S11, Supporting Information) also indicate nearly ohmic contact between the electrodes and the 2D perovskite films, which is advantageous for charge collection. For the BTMA-Pb perovskite photodetector, the dark current is found to be 1×10^{-13} A under a bias of 1.5 V. But, the NMA-Pb perovskite device shows a smaller dark current, which is as low as 3×10^{-14} A under the same bias. The lower crystallinity and film quality of NMA-Pb perovskite and the higher quantum confinement effect caused by NMA spacers with smaller dipole moments hinder the flow of charges. The time-dependent photoresponse characteristics were also studied. The results of current–time (I–t) measurement under a light intensity of 121 mW cm^{-2} and 1.5 V bias voltage are shown in Figure 3c. The on/off photoswitching characteristics

of BTMA-Pb and NMA-Pb perovskite photodetectors are stable and invertible. Figure 3d displays the curves correlating various light intensities with the corresponding photocurrent, exhibiting a clear linear relationship,[33] which is a typical phenomenon in semiconductor-based photodetectors because of the unique process of generation, trapping, and recombination of electron–hole pairs. The linear dynamic range (LDR) can be calculated using the equation: LDR = $20\log(P_{upper}/P_{lower})$, where P_{lower} and P_{upper} represent the lowest and highest light intensities used in this work. The BTMA-Pb and NMA-Pb perovskite devices display an obvious linear response from 0.0122 to 121.89 mW cm^{-2}, which indicates a large LDR of 80 dB. The responsivity (R) is an important parameter characterizing the performance of photodetectors and is determined by the formula of $R = I_p/\Phi S$, where I_p is the photocurrent, Φ is the light intensity, S is the

**ADVANCED
SCIENCE NEWS**

www.advancedsciencenews.com

**ADVANCED
FUNCTIONAL
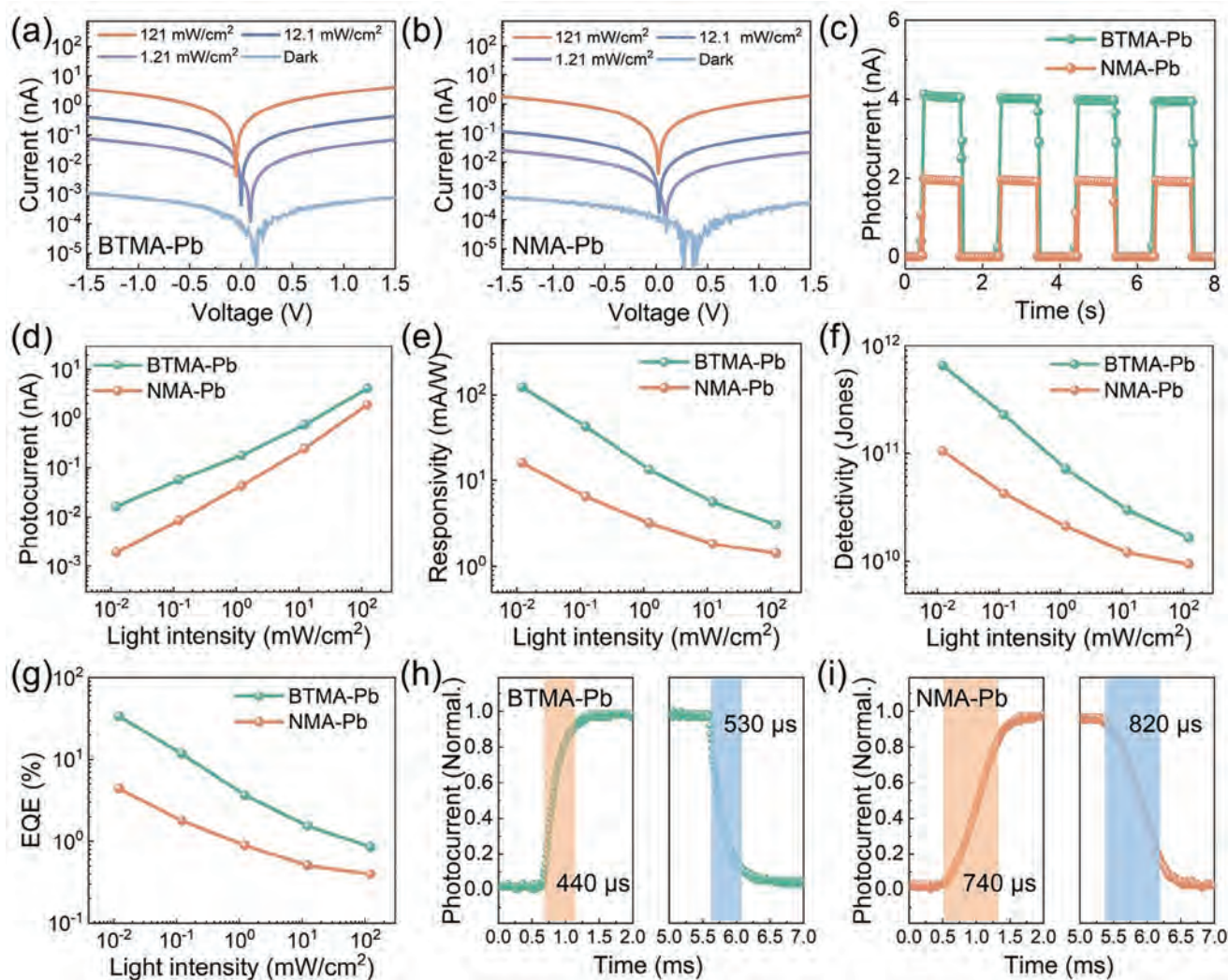MATERIALS**

www.afm-journal.de

Figure 3. a,b) I–V curves of photodetectors based on BTMA-Pb and NMA-Pb films with varying illumination intensities. c) On-off switching curves of the BTMA-Pb and NMA-Pb perovskite-based photodetectors. d–g) The relationship of light intensity with d) photocurrent, e) responsivity, f) detectivity, and g) EQE of the BTMA-Pb and NMA-Pb perovskite photodetectors. Determination of the rise and fall times of the h) BTMA-Pb and i) NMA-Pb perovskite photodetectors at a bias of 1.5 V.

active area of the photodetector.[30] As illustrated in Figure 3e, the BTMA-Pb perovskite photodetector exhibits a superior R value of 122 mA W^{-1}, which is significantly higher compared to the NMA-Pb perovskite device (15 mA W^{-1}) under a light intensity of 0.0121 mW cm^{-2}. Detectivity (D^*) characterizes the weakest level of light that the device can detect, which is determined by the responsivity and noise of the photodetector. The D^* is calculated by the formula of $D^* = S^{1/2}/NEP$, where NEP is the noise equivalent power which can be calculated by the formula of NEP $= I_n/R$ (I_n is the current noise spectral density). Generally, there are three contributions to noise that limit D^*: the shot noise from dark current, Johnson noise, and thermal fluctuation "flicker" noise. For simply estimating the D^* value, assuming that shot noise from the dark current is the major contributor to the total noise, the shot noise current of the detector can be evaluated by $i_n = (2eI_{dark}\Delta f)^{1/2}$, where I_{dark} is the dark current, Δf is the electrical bandwidth and e is the electronic charge.[34]

Therefore, the specific detectivity (D^*) can be calculated by the formula of $D^* = S^{1/2}/NEP = RS^{1/2}/(2eI_{dark})^{1/2}$. The most significant D^* values are calculated as 6×10^{11} and 1×10^{11} Jones at 0.0121 mW cm^{-2} light intensity for BTMA-Pb and NMA-Pb perovskite photodetectors, respectively, as shown in Figure 3f. Moreover, according to the formula of EQE $= hcR/e\lambda$, where h represents the Planck's constant, c represents the velocity of light and λ represents the wavelength of the incident light, the external quantum efficiency (EQE) of photodetectors can also be obtained. Figure 3g shows that the maximum EQE values of perovskite device samples based on BTMA and NMA spacers can reach 33% and 4%, respectively. Similar to the R, the D^* and EQE values of BTMA-Pb devices are higher than those of NMA-Pb devices. The better performance for BTMA-Pb perovskite photodetector can be attributed to the great crystallinity and high-quality film, as well as the weakened quantum confinement effect in 2D RP perovskite lattices. These factors are in favor of the transport of the

photogenerated carriers. In addition, a short response time is essential for high-performance photodetectors. Accordingly, high-resolution I–t curve testing was employed to study the response rate of the device samples at the light intensity of 121 mW cm^{-2}. Generally, the response time is characterized by two key metrics: the rise time and the decay time, which are defined as the duration required for the current to escalate from 10% to 90% and diminish from 90% to 10% of the peak value, respectively. As depicted in Figure 3h,i, the BTMA-Pb perovskite photodetector exhibits a faster rise and decay time of 440 and 530 μs, respectively, in contrast to the NMA-Pb perovskite device, where rise and decay times of 740 and 820 μs are observed. The higher response speed of BTMA-Pb devices is profiting from the increased charge transport ability. Consequently, all these improved metrics, including responsivity, detectivity, EQE, and response time, demonstrate the superior performance of the BTMA-Pb perovskite photodetector device.

In addition, to further study the quality of BTMA-Pb and NMA-Pb films, we performed the space-charge-limited current (SCLC) measurement as shown in Figure S12, Supporting Information. It can be seen that with the bias voltage increasing, ohmic, trap-filled limit (TLF), and Child's regions are clearly separated.[35,36] The V_{TFL} (related to the trap state n_{trap}) for BTMA-Pb and NMA-Pb films are 1.9 and 4.38 V, respectively. The n_{trap} can be calculated from the formula of $n_{trap} = 2\epsilon\epsilon_0 V_{TFL}/eL^2$, where ϵ is the relative dielectric constant, ϵ_0 is the vacuum permittivity, and L is the length between two electrodes. As a result, the BTMA-Pb film displays a trap density of 3.4×10^{12} cm^{-3}, which is lower than that of NMA-Pb film (7.2×10^{12} cm^{-3}), indicating higher film quality of BTMA-Pb perovskite film. Also, by fitting the third segment (Child' region) of the SCLC curve with the formula of $J = 9\epsilon\epsilon_0\mu V^2/8L^3$ (J is the current density), we obtained the carrier mobility, μ, of BTMA-Pb and NMA-Pb films being ≈5.16 × 10^{-3} and ≈ 3.27×10^{-4} cm^2 V^{-1} s^{-1}, respectively.

The stability of perovskite materials is critical in determining their potential for widespread commercialization. Therefore, to explore the stability of BTMA-Pb and NMA-Pb films under various external environmental stimuli, these films were exposed to high humidity and temperature conditions, and their changes were monitored over time using XRD measurements. For the moisture stability study, these films were placed in an air environment with a constant relative humidity (RH) of 80 ± 5 % at room temperature. The results depicted in **Figure 4**a reveal that after 48 h, the NMA-Pb film changes to be pale, and numerous impurity diffraction peaks arise, accompanied by a noticeable widening of the spacing between the main peaks. After 144 h, no further changes occurred in the diffraction peaks of NMA-Pb films. According to previous reports, these results are possibly caused by the intrusion of water molecules into the perovskite lattices.[37] Due to the weak interaction of NMA spacers with inorganic octahedral sheets, water molecules in a humid environment can more easily intrude between the NMA spacers and I atoms of PbI$_6$ frameworks to form hydrogen bonds with NH$_3^{2+}$ of NMA cations, thereby producing a hydrate phase. In contrast, BTMA-Pb films retain their initial diffraction peaks even after 192 hours, indicating their great humidity stability, which can be attributed to the enhanced interaction that has been demonstrated above between BTMA spacers and PbI$_6$ octahedrons (Figure 4d). Subsequently, thermal stability was evaluated by placing NMA-

Pb and BTMA-Pb films on a hot plate at 80 °C. The results illustrated in Figure 4b,e manifest that the color of the NMA-Pb films gradually fades to colorless within 27 h, and correspondingly, the XRD peaks gradually disappear, suggesting that the perovskite lattices were decomposed. Conversely, no significant change was observed for

BTMA-Pb film after the same period, suggesting its outstanding thermal stability. In addition, long-term on/off light-switching stability is also crucial for photodetectors as they are expected to be operated under persistent illumination. Therefore, we also investigated the light stability for photodetectors based on BTMA-Pb and NMA-Pb films. The measurement was conducted by continuously recording the I–t curves of the photodetector devices for 5000 s under the laser illumination with a light intensity of 60 mW cm^{-2} at a bias voltage of 1.5 V, as shown in Figure 4c,f. Figure 4f shows that the intensity of the photocurrent for BTMA-Pb photodetector does not exhibit a significant decrease after 5000 s. However, for the NMA-Pb device, the current magnitude drops by two orders of magnitude, indicating its poor stability. All of these findings suggest that, compared to NMA-Pb film and its device, BTMA-Pb exhibits superior humidity, heat, and illumination stability, benefiting from the enhanced interaction brought by the thiophene group between organic layers and inorganic layers in 2D perovskite lattices. Although the above photodetector based on the BTMA-Pb perovskite has achieved good performance, there is still much room for improvement. In order to further improve the device performance of the BTMA-Pb perovskite, we prepared the photodetector using asymmetric aluminum–gold (Al–Au) nanogap electrodes.[25] The SEM images of the Al–Au nanogap electrode interface and the statistical mean for the gap are shown in **Figure 5**a and Figure S15, Supporting Information (the diameter of the Au electrode is 600 μm, and the gap between the Au electrode and the Al electrode is approximately 10 nm). It is noted that the significant reduction in the distance between the electrodes inevitably leads to the promotion of charge collection, which can greatly enhance device performance. Moreover, using asymmetric electrodes can also form the Schottky barriers (the energy band alignment is shown in

Figure S14, Supporting Information) at the opposite contact between the Al/Au electrodes and the BTMA-Pb perovskite film, thereby endowing the photodetector with self-powered characteristics.[38] The nanogap photodetector is illuminated by a 450 nm laser. Similar to the measurements for photodetector devices with traditional structures, the I–V curves are studied under different light intensities, as Figure 5b shows. The results show that the dark current is below 0.04 nA under the bias from -1 to 1 V. Besides, it is unsurprising that the open circuit voltage (V_{OC}) displays a noticeable shift of approximately 0.6 V from the zero point, which proves the presence of the Schottky barriers at the interfaces between the perovskite film and the electrodes. The performance of the nanogap device with bias and without bias (self-power) was further studied. The I–t curves of the BTMA-Pb perovskite nanogap photodetector under an intensity of 13.7 mW cm^{-2} were recorded and shown in Figure 5c. It can be seen that under a bias voltage of 1 V, the maximum photocurrent of the nanogap photodetector can reach the nanoampere level. In contrast, under zero bias, the photocurrent is an order of magnitude smaller. It is noted that at the beginning of every excitation, the photocurrent rose to a high value and then
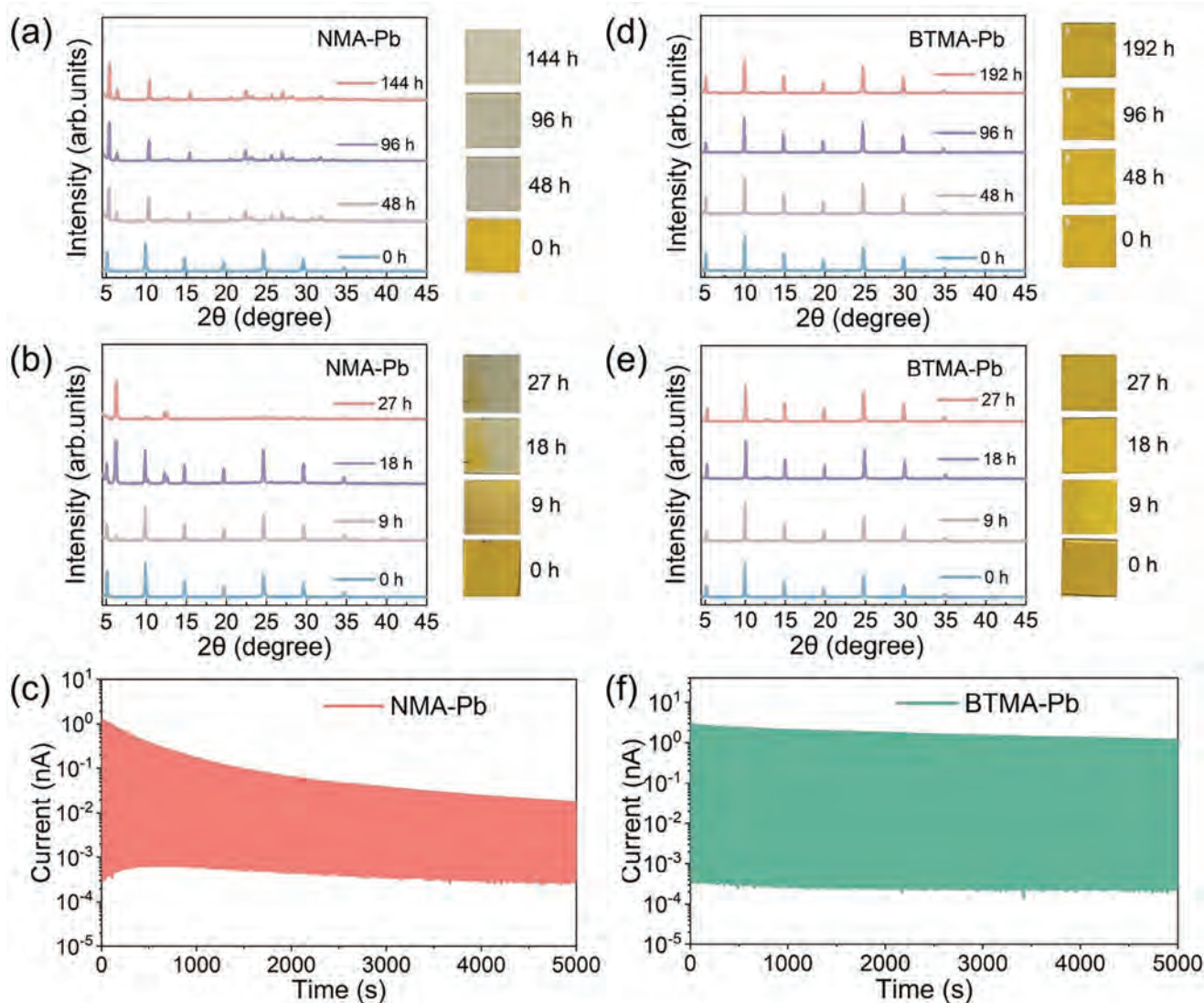
**ADVANCED
SCIENCE NEWS**

www.advancedsciencenews.com

**ADVANCED
FUNCTIONAL
MATERIALS**

www.afm-journal.de

Figure 4. a,d) Moisture stability test under 80 ± 5% RH at room temperature monitored using XRD measurements and optical microscopy images for the a) NMA-Pb and d) BTMA-Pb films. b,e) Heat stability test at 80 °C monitored using XRD measurements and optical microscopy images for b) the NMA-Pb and e) BTMA-Pb films. c,f) Long-time operation stability test of c) the NMA-Pb and f) BTMA-Pb perovskite photodetectors.

rapidly decreased to a stable state. The appearance of this sharp peak for photocurrent is owing to the huge temperature change of perovskite materials.[39–41] Specifically, the initial excitation for perovskite film results in a significant temperature change because the temperature of the material before excitation is low. However, during subsequent continuous excitation, the material always remains at a high and stable temperature. Besides, as the light intensity increases from low to high, the photocurrent of the nanogap detector exhibits a typical linear change, consistent with other photoelectric semiconductor detectors (Figure 5d). The characteristic of the on/off switching is also distinct and reversible. Furthermore, the R, D^*, and EQE of the nanogap photodetectors can also be calculated using the formulas mentioned above. All these results also present a linear relationship corresponding to the light intensity. Figure 5e–g shows the values of R, D^*, and EQE of nanogap photodetectors at 1 V bias are

as high as 314 A W^{-1}, 3.4 × 10^{13} Jones, and 865%, respectively, larger than those of BTMA-Pb perovskite photodetector with traditional device structure. These improvements are attributable to the nanogap electrodes and their higher charge collection capability. The rise and decay times of the nanogap photodetector were measured under 13.7 mW cm^{-2} light intensity and the results are 448 and 424 µs, as shown in Figure 5h. It is worth mentioning that the response speed is close to the traditional BTMA-Pb perovskite photodetectors, which can be attributed to the Al$_2$O$_3$ insulation layer forming on the surface of the Al electrode and the different work functions of Au and Al electrodes.[51,52] The comparison of the parameters of this nanogap photodetector with those of other halide perovskites-based photodetector devices is also shown in **Table 1**, demonstrating the superior performance of our nanogap device. Moreover, the nanogap photodetector based on the BTMA-Pb perovskite film also displays
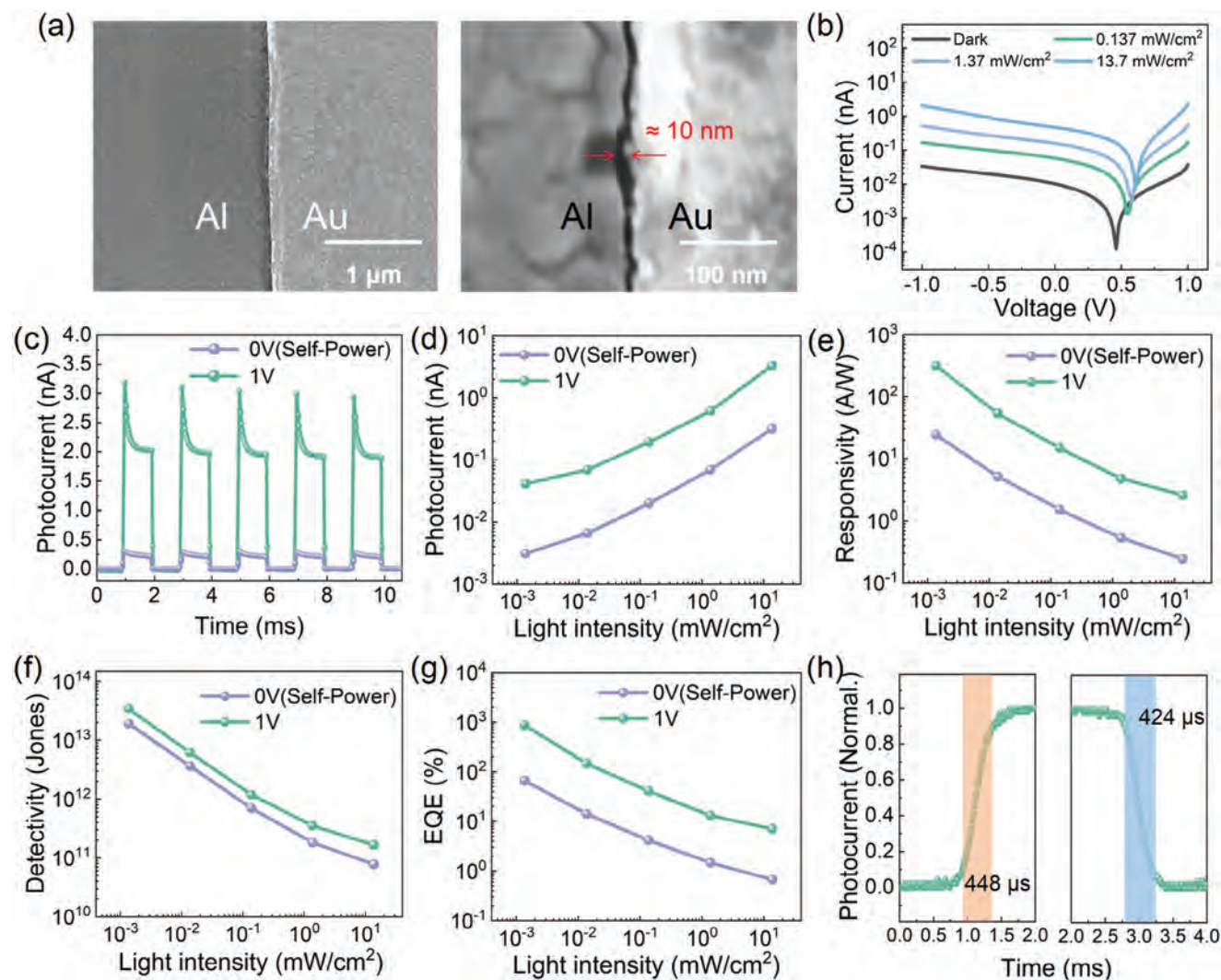
Figure 5. a) SEM images of Al–Au nanogap electrodes interface under different scale bars. b) I–V curves of the BTMA-Pb nanogap photodetector with varying illumination intensities. c) On-off switching curves of the BTMA-Pb based nanogap photodetector with 1 V bias and without bias. d–g) The relationship of light intensity with d) photocurrent, e) responsivity, f) detectivity, and g) EQE of the BTMA-Pb perovskite nanogap photodetector with 1 V bias and without bias. (h) Determination of the rise and fall times of the BTMA-Pb-based nanogap photodetector at a bias of 1 V.

Table 1. Comparison of different figures of merits for halide perovskites-based photodetectors.

Perovskites	Bias [V]	λ [nm]	R [mA W^{-1}]	D* [Jones]	Rise/decay time [ms]	Refs.
$CH_3NH_3PbI_3$ epitaxial film	5	520	2.07×10^4	$6.5 \times 10^{13\,a)}$	0.017/0.018	[42]
$(PEA)_2PbI_4$ crystal	5	Solar light	5	$1.07 \times 10^{13\,a)}$	N/A	[43]
$MAPbI_{3-x}Cl_x$ film	0	632	1.1×10^5	$3.53 \times 10^{14\,a)}$	230/380	[44]
$CsPbCl_3$ single microplatelet	5	390	450	$1.0 \times 10^{11\,b)}$	8/7	[45]
$(C_4H_9NH_3)_2(MA)_3Pb_4I_{13}$	20	525	4400	$5.0 \times 10^{12\,a)}$	0.0036/0.0035	[46]
$CsPbBr_3$ QDs	2	405	2.4×10^4	$8.9 \times 10^{13\,a)}$	4700/2300	[47]
$MAPbI_3$ Microwires	10	White light	1.3×10^4	$5.25 \times 10^{12\,a)}$	0.08/0.24	[48]
$(iBA)_2(MA)_{n-1}Pb_nI_{3n+1}$	1.5	532	120	N/A	16/15	[49]
$(C_6H_5(CH_2)_3NH_3)_3Pb_2I_7$	5	515	N/A	$1.2 \times 10^{10\,a)}$	0.85/0.78	[50]
$BTMA_2PbI_4$	1	450	3.14×10^5	$3.4 \times 10^{13\,a)}$	0.448/0.424	This work

Different formula for calculating detectivity($D*$): $^{a)}$ $D* = RS^{1/2}/(2eI_{dark})^{1/2}$, where e is the electronic charge, S is the effective area of the photodetector, R is the responsivity, and I_{dark} is the dark current; $^{b)}$ $D* = R(\Delta fS)^{1/2}/(I_n)^{1/2}$, where S is the effective area of the photodetector, Δf is the electrical bandwidth, R is the responsivity, and i_n is the noise current.

excellent performance in the self-powered mode. Under this mode, the R value of nanogap photodetectors can reach 24 A W^{-1}, which is still three orders of magnitude higher than that of the device with a traditional structure using the same 2D perovskite material. The values of D^* and EQE also present large values, which are 1.9×10^{13} Jones and 66%, as shown in Figure 5e–g. Table S1, Supporting Information, shows the comparison of previous self-powered halide perovskite photodetectors and our work, also indicating the excellent self-powered characteristics of the BTMA-Pb nanogap detector. All these data indicate that the BTMA-Pb perovskite photodetectors fabricated with asymmetric nanogap electrodes can achieve excellent photoelectric performance while also endowing the photodetector with great self-powered characteristics.

3. Conclusion

In conclusion, a new multiple aromatic ring spacer BTMA was designed and successfully employed to form one new kind of 2D halide perovskites. Our results suggest that the BTMA spacer has a larger dipole moment than the NMA spacer, and the presence of S atoms or thiophene can enhance the interaction between spacer layers and inorganic octahedral layers, thereby stabilizing the perovskite lattices. Contrasted with NMA-Pb film, BTMA-Pb film exhibits a dense surface without observable cracks. Benefiting from the weakened quantum confinement effect brought by the higher polarity of BTMA spacer and enhanced interaction between organic layers and inorganic layers, better photoelectric performance is demonstrated for BTMA-Pb perovskite photodetector compared with the device based on NMA-Pb perovskite. Meanwhile, excellent stability under moisture, heat and illumination conditions was also observed for the BTMA-Pb film and device. More importantly, BTMA-Pb perovskite photodetector with nanogap electrodes dramatically enhances its performance and self-powered characteristics. The maximum values of R, D^*, and EQE for nanogap devices can reach 314 A W^{-1}, 3.4 $\times 10^{13}$ Jones, and 865%, respectively. The work creates new research avenues towards more stable and higher-performance 2D halide perovskite-based optoelectronic devices.

Supporting Information

Supporting Information is available from the Wiley Online Library or from the author.

Acknowledgements

Conflict of Interest

The authors declare no conflict of interest.

Data Availability Statement

The data that support the findings of this study are available from the corresponding author upon reasonable request.

[1] L. K. Ono, Y. Qi, S. Liu, *Joule* **2018**, *2*, 1961.
[2] J. J. Yoo, G. Seo, M. R. Chua, T. G. Park, Y. Lu, F. Rotermund, Y. K. Kim, C. S. Moon, N. J. Jeon, J. P. Correa-Baena, V. Bulovic, S. S. Shin, M. G. Bawendi, J. Seo, *Nature* **2021**, *590*, 587.
[3] A. Ren, H. Lai, X. Hao, Z. Tang, H. Xu, B. M. F. Yu Jeco, K. Watanabe, L. Wu, J. Zhang, M. Sugiyama, J. Wu, D. Zhao, *Joule* **2020**, *4*, 1263.
[4] M. A. Green, A. Ho-Baillie, H. J. Snaith, *Nat. Photonics* **2014**, *8*, 506.
[5] A. K. Jena, A. Kulkarni, T. Miyasaka, *Chem. Rev.* **2019**, *119*, 3036.
[6] N. J. Jeon, J. H. Noh, Y. C. Kim, W. S. Yang, S. Ryu, S. I. Seok, *Nat. Mater.* **2014**, *13*, 897.
[7] T. Leijtens, G. E. Eperon, N. K. Noel, S. N. Habisreutinger, A. Petrozza, H. J. Snaith, *Adv. Energy Mater.* **2015**, *5*, 1500963.
[8] K. Miyano, M. Yanagida, N. Tripathi, Y. Shirai, *J. Phys. Chem. Lett.* **2016**, *7*, 2240.
[9] C. Liang, H. Gu, Y. Xia, Z. Wang, X. Liu, J. Xia, S. Zuo, Y. Hu, X. Gao, W. Hui, L. Chao, T. Niu, M. Fang, H. Lu, H. Dong, H. Yu, S. Chen, X. Ran, L. Song, B. Li, J. Zhang, Y. Peng, G. Shao, J. Wang, Y. Chen, G. Xing, W. Huang, *Nat. Energy* **2020**, *6*, 38.
[10] M. Shao, T. Bie, L. Yang, Y. Gao, X. Jin, F. He, N. Zheng, Y. Yu, X. Zhang, *Adv. Mater.* **2022**, *34*, 2107211.
[11] I. C. Smith, E. T. Hoke, D. Solis-Ibarra, M. D. McGehee, H. I. Karunadasa, *Angew. Chem., Int. Ed. Engl.* **2014**, *53*, 11232.
[12] J. Shi, Y. Gao, X. Gao, Y. Zhang, J. Zhang, X. Jing, M. Shao, *Adv. Mater.* **2019**, *31*, 1901673.
[13] J. Hu, I. W. H. Oswald, H. Hu, S. J. Stuard, M. M. Nahid, L. Yan, Z. Chen, H. Ade, J. R. Neilson, W. You, *ACS Mater. Lett.* **2019**, *1*, 171.
[14] R. Wang, X. Dong, Q. Ling, Q. Fu, Z. Hu, Z. Xu, H. Zhang, Q. Li, Y. Liu, *ACS Mater. Lett.* **2022**, *7*, 3656.
[15] X. Hong, T. Ishihara, A. V. Nurmikko, *Phys. Rev. B: Condens. Matter Mater. Phys.* **1992**, *45*, 6961.
[16] E. A. Muljarov, S. G. Tikhodeev, N. A. Gippius, T. Ishihara, *Phys. Rev. B: Condens. Matter Mater. Phys.* **1995**, *51*, 14370.
[17] W. Fu, H. Liu, X. Shi, L. Zuo, X. Li, A. K. Y. Jen, *Adv. Funct. Mater.* **2019**, *29*, 1900221.
[18] J. M. Hoffman, X. Che, S. Sidhik, X. Li, I. Hadar, J. C. Blancon, H. Yamaguchi, M. Kepenekian, C. Katan, J. Even, C. C. Stoumpos, A. D. Mohite, M. G. Kanatzidis, *J. Am. Chem. Soc.* **2019**, *141*, 10661.
[19] J. M. Hoffman, C. D. Malliakas, S. Sidhik, I. Hadar, R. McClain, A. D. Mohite, M. G. Kanatzidis, *Chem. Sci.* **2020**, *11*, 12139.
[20] X. Dong, M. Chen, R. Wang, Q. Ling, Z. Hu, H. Liu, Y. Xin, Y. Yang, J. Wang, Y. Liu, *Adv. Energy Mater.* **2023**, *13*, 2301006.
[21] J. V. Passarelli, D. J. Fairfield, N. A. Sather, M. P. Hendricks, H. Sai, C. L. Stern, S. I. Stupp, *J. Am. Chem. Soc.* **2018**, *140*, 7313.
[22] R. Wang, X. Dong, Q. Ling, Z. Hu, Y. Gao, Y. Chen, Y. Liu, *Angew. Chem., Int. Ed. Engl.* **2023**, *62*, 202314690.
[23] Z. Xu, D. Lu, F. Liu, H. Lai, X. Wan, X. Zhang, Y. Liu, Y. Chen, *ACS Nano* **2020**, *14*, 4871.
[24] H. Yao, Z. Li, C. Shi, Y. Xu, Q. Wang, Z. Li, G. Peng, Y. Lei, H. Wang, Z. Ci, Z. Jin, *Adv. Funct. Mater.* **2022**, *32*, 2205029.
[25] D. G. Georgiadou, J. Semple, A. A. Sagade, H. Forstén, P. Rantakari, Y.-H. Lin, F. Alkhalil, A. Seitkhan, K. Loganathan, H. Faber, T. D. Anthopoulos, *Nat. Electron.* **2020**, *3*, 718.

[26] K. Loganathan, A. D. Scaccabarozzi, H. Faber, F. Ferrari, Z. Bizak, E. Yengel, D. R. Naphade, M. Gedda, Q. He, O. Solomeshch, B. Adilbekova, E. Yarali, L. Tsetseris, K. N. Salama, M. Heeney, N. Tessler, T. D. Anthopoulos, *Adv. Mater.* **2022**, *34*, 2108524.

[27] Y. Yan, S. Yu, A. Honarfar, T. Pullerits, K. Zheng, Z. Liang, *Adv. Sci.* **2019**, *6*, 1900548.

[28] J. Liang, Z. Zhang, Y. Huang, Q. Xue, Y. Zheng, X. Wu, C. Tian, Y. Zhang, Y. Wang, Z. Chen, C. C. Chen, *Adv. Funct. Mater.* **2022**, *32*, 2207177.

[29] Y. Qin, H. Zhong, J. J. Intemann, S. Leng, M. Cui, C. Qin, M. Xiong, F. Liu, A. K. Y. Jen, K. Yao, *Adv. Energy Mater.* **2020**, *10*, 1904050.

[30] H. P. Wang, S. Li, X. Liu, Z. Shi, X. Fang, J. H. He, *Adv. Mater.* **2021**, *33*, 2003309.

[31] K. Z. Du, Q. Tu, X. Zhang, Q. Han, J. Liu, S. Zauscher, D. B. Mitzi, *Inorg. Chem.* **2017**, *56*, 9291.

[32] W. Tress, N. Marinova, T. Moehl, S. M. Zakeeruddin, M. K. Nazeeruddin, M. Grätzel, *Energy Environ. Sci.* **2015**, *8*, 995.

[33] F. Binet, J. Y. Duboz, E. Rosencher, F. Scholz, V. Härle, *Appl. Phys. Lett.* **1996**, *69*, 1202.

[34] L. Dou, Y. M. Yang, J. You, Z. Hong, W. H. Chang, G. Li, Y. Yang, *Nat. Commun.* **2014**, *5*, 5404.

[35] R. H. Bube, *J. Appl. Phys.* **1962**, *33*, 1733.

[36] V. M. Le Corre, E. A. Duijnstee, O. El Tambouli, J. M. Ball, H. J. Snaith, J. Lim, L. J. A. Koster, *ACS Energy Lett.* **2021**, *6*, 1087.

[37] A. M. A. Leguy, Y. Hu, M. Campoy-Quiles, M. I. Alonso, O. J. Weber, P. Azarhoosh, M. van Schilfgaarde, M. T. Weller, T. Bein, J. Nelson, P. Docampo, P. R. F. Barnes, *Chem. Mater.* **2015**, *27*, 3397.

[38] D. G. Georgiadou, Y. H. Lin, J. Lim, S. Ratnasingham, M. A. McLachlan, H. J. Snaith, T. D. Anthopoulos, *Adv. Funct. Mater.* **2019**, *29*, 1901371.

[39] X. Zheng, M. Dong, Q. Li, Y. Liu, X. Di, X. Lu, J. Meng, Z. Li, *Adv. Opt. Mater.* **2024**, *12*, 2303177.

[40] Y. Wang, L. Zhu, Y. Feng, Z. Wang, Z. L. Wang, *Adv. Funct. Mater.* **2018**, *29*, 1807111.

[41] Z. Li, C. Ji, Y. Fan, T. Zhu, S. You, J. Wu, R. Li, Z. K. Zhu, P. Yu, X. Kuang, J. Luo, *J. Am. Chem. Soc.* **2023**, *145*, 25134.

[42] L. Ji, H. Y. Hsu, J. C. Lee, A. J. Bard, E. T. Yu, *Nano Lett.* **2018**, *18*, 994.

[43] C. H. Lin, B. Cheng, T. Y. Li, J. R. D. Retamal, T. C. Wei, H. C. Fu, X. Fang, J. H. He, *ACS Nano* **2019**, *13*, 1168.

[44] S. V. N. Pammi, R. Maddaka, V.-D. Tran, J.-H. Eom, V. Pecunia, S. Majumder, M.-D. Kim, S. G. Yoon, *Nano Energy* **2020**, *74*, 104872.

[45] P. Gui, H. Zhou, F. Yao, Z. Song, B. Li, G. Fang, *Small* **2019**, *15*, e1902618.

[46] W. Li, Q. Wu, L. Lu, Y. Tian, H. Luo, Y. Yun, S. Jiang, M. Chen, C. Li, *J. Mater Chem. C* **2023**, *11*, 3314.

[47] L. Zhou, K. Yu, F. Yang, H. Cong, N. Wang, J. Zheng, Y. Zuo, C. Li, B. Cheng, Q. Wang, *J. Mater. Chem. C* **2017**, *5*, 6224.

[48] Y. Chen, J. Zhang, J. Zhou, Y. Chu, B. Zhou, X. Wu, J. Huang, *Adv. Opt. Mater.* **2018**, *6*, 1800469.

[49] R. Dong, C. Lan, X. Xu, X. Liang, X. Hu, D. Li, Z. Zhou, L. Shu, S. Yip, C. Li, S. W. Tsang, J. C. Ho, *ACS Appl. Mater. Interfaces* **2018**, *10*, 19019.

[50] X. Fu, S. Jiao, Y. Jiang, L. Li, X. Wang, C. Zhu, C. Ma, H. Zhao, Z. Xu, Y. Liu, W. Huang, W. Zheng, P. Fan, F. Jiang, D. Zhang, X. Zhu, X. Wang, A. Pan, *ACS Appl. Mater. Interfaces* **2020**, *12*, 2884.

[51] Y. Zhao, C. Li, L. Shen, *InfoMat* **2019**, *1*, 164.

[52] M. L. Lee, J. K. Sheu, W. C. Lai, Y. K. Su, S. J. Chang, C. J. Kao, C. J. Tun, M. G. Chen, W. H. Chang, G. C. Chi, J. M. Tsai, *J. Appl. Phys.* **2003**, *94*, 1753.